11-8-2016

Observation and Modeling of Gravity Wave Propagation through Reflection and Critical Layers above Andes Lidar Observatory at Cerro Pachón, Chile

Bing Cao
Embry-Riddle Aeronautical University, caob@erau.edu

Christopher J. Heale
Embry-Riddle Aeronautical University, HEALEC@erau.edu

Yafang Guo
Embry-Riddle Aeronautical University, guoy1@erau.edu

Alan Z. Liu
Embry-Riddle Aeronautical University, liuz2@erau.edu

Jonathan B. Snively
Embry-Riddle Aeronautical University, snivelyj@erau.edu

AGU PUBLICATIONS

JGR

Journal of Geophysical Research: Atmospheres

RESEARCH ARTICLE
10.1002/2016JD025173

Key Points:
- A gravity wave event with large vertical wind oscillations was observed by a lidar and an airglow imager
- A numerical simulation was able to reproduce and help to interpret the key features of the wave events
- Observation and modeling show that the event undergoes partial reflection, transmission, and critical layer filtering

Correspondence to:
B. Cao,
caob@my.erau.edu

Citation:
Cao, B., C. J. Heale, Y. Guo, A. Z. Liu, and J. B. Snively (2016), Observation and modeling of gravity wave propagation through reflection and critical layers above Andes Lidar Observatory at Cerro Pachón, Chile, *J. Geophys. Res. Atmos.*, *121*, 12,737–12,750, doi:10.1002/2016JD025173.

Received 1 APR 2016
Accepted 18 OCT 2016
Accepted article online 24 OCT 2016
Published online 8 NOV 2016

Observation and modeling of gravity wave propagation through reflection and critical layers above Andes Lidar Observatory at Cerro Pachón, Chile

Bing Cao[1], Christopher J. Heale[1], Yafang Guo[1], Alan Z. Liu[1], and Jonathan B. Snively[1]

[1]Center for Space and Atmospheric Research, Department of Physical Sciences, Embry-Riddle Aeronautical University, Daytona Beach, Florida, USA

Abstract A complex gravity wave event was observed from 04:30 to 08:10 UTC on 16 January 2015 by a narrow-band sodium lidar and an all-sky airglow imager located at Andes Lidar Observatory (ALO) in Cerro Pachón (30.25°S, 70.73°W), Chile. The gravity wave packet had a period of 18–35 min and a horizontal wavelength of about 40–50 km. Strong enhancements of the vertical wind perturbation, exceeding 10 m s^{-1}, were found at ~90 km and ~103 km, consistent with nearly evanescent wave behavior near a reflection layer. A reduction in vertical wavelength was found as the phase speed approached the background wind speed near ~93 km. A distinct three-layered structure was observed in the lidar data due to refraction of the wave packet. A fully nonlinear model was used to simulate this event, which successfully reproduced the amplitudes and layered structure seen in observations. The model results provide dynamical insight, suggesting that a double reflection occurring at two separate heights caused the large vertical wind amplitudes, while the three-layered structure in the temperature perturbation was a result of relatively stable regions at those altitudes. The event provides a clear perspective on the filtering processes to which short-period, small-scale gravity waves are subject in mesosphere and lower thermosphere.

1. Introduction

Atmospheric gravity waves (GWs) are ubiquitous in the atmosphere and occur at a variety of spatial and temporal scales. GWs are mostly generated in the lower atmosphere by convection, orography, and wind shear, then propagate upward conservatively [*Fritts and Alexander*, 2003, and references therein]. In the mesopause region, these GWs can either dissipate through saturation or critical layers [*Lindzen*, 1981; *Dunkerton and Fritts*, 1984; *Fritts and Rastogi*, 1985; *Franke and Robinson*, 1999; *Vadas et al.*, 2003] or propagate continuously to higher altitudes and dissipate via viscosity. The corresponding momentum flux will be transferred from the wave field to the mean flow in these cases. This process plays an important role in driving the global scale Brewer-Dobson meridional circulation [*Holton et al.*, 1995; *Li et al.*, 2008; *Cohen et al.*, 2014] and influences the atmospheric thermal balance, leading to a dynamical rather than radiative equilibrium state in the middle atmosphere [*Gierasch et al.*, 1970; *Andrews et al.*, 1987; *Liou*, 2002]. At small scales, GWs contribute to the instability and turbulence processes in the atmosphere [*Fritts*, 1984; *Fritts et al.*, 2013]. In the thermosphere and ionosphere, GWs contribute to irregularities and traveling ionospheric disturbances [*Fritts and Lund*, 2011; *Liu and Vadas*, 2013].

Many remote sensing instruments have been developed to observe atmospheric processes, of which lidar and airglow imager are used extensively to study GW characteristics and their effects in mesosphere and lower thermosphere (MLT) region [*Taylor*, 1997; *Hu et al.*, 2002; *Espy et al.*, 2006; *Li et al.*, 2007; *Lu et al.*, 2009; *Li et al.*, 2011; *Chen et al.*, 2013; *Fritts et al.*, 2014; *Lu et al.*, 2015a; *Chen et al.*, 2016]. In addition to these observational techniques, many mesoscale numerical models [*Zhang and Yi*, 2002; *Snively et al.*, 2007; *Yu and Hickey*, 2007; *Huang et al.*, 2012; *Liu et al.*, 2013; *Heale et al.*, 2014a] are also used to investigate GW dynamics by simulating the propagation, interaction, and dissipation of GWs in given background atmosphere, thus providing a valuable tool to understand the wave processes with nearly 4-D (temporal and spatial) data sets. Studies based on these observations and modeling work have contributed to our understanding of GW characteristics such as scales, periods, phase speeds, possible sources, and their propagation and dissipation processes.

Lidar measurements provide high-resolution profiles at a single location and therefore only resolve GW vertical structures. Airglow imagers provide GW horizontal information retrieved from the airglow layers over a

narrow portion of the atmosphere. For reliable estimates of wave parameters and characterization of the dissipation process, observations from multiple instruments that are complementary in resolving GWs are needed. Such simultaneous observations from lidars and airglow imagers enable the investigation of small-scale bore/ripple structures and instabilities associated with GW breaking [*Hecht et al.*, 1997; *She et al.*, 2004; *Li et al.*, 2005; *Smith et al.*, 2005; *Cai et al.*, 2014], estimation of GW momentum flux [*Fritts et al.*, 2014], and GW intrinsic characteristics [*Taylor et al.*, 1995; *Suzuki et al.*, 2013a; *Lu et al.*, 2015b]. Most recently, *Bossert et al.* [2014] used coordinated sodium lidar and Advanced Mesospheric Temperature Mapper (AMTM) measurements to investigate GWs at Arctic Lidar Observatory for Middle Atmosphere Research (ALOMAR) Observatory, Norway. The squared vertical wave number m^2 was calculated for well-characterized GWs from the lidar and AMTM data and used as a diagnosis for the altitude range at which GWs could freely propagate, become ducted or evanescent. Using similar sodium lidar and Mesospheric Temperature Mapper (MTM) observations at Logan, Utah, *Yuan et al.* [2016] studied a GW packet with a broad spectrum propagating in the presence of a larger-scale wave motion, leading to time- and altitude-dependent periods and vertical wavelengths. The numerical model of *Snively and Pasko* [2008] was used to simulate the wave packet and produced remarkable similarities between the observations and simulation results under relatively idealized conditions.

The linearized GW theory has long predicted reflection, critical levels, and ducting. Several studies have used numerical models to investigate the characteristics of reflection and transmission of GW packets in atmosphere with vertically or horizontally sheared winds and vertically varying temperature, including occurrences of waves trapped between two reflection layers known as ducts [*Walterscheid et al.*, 2001; *Snively et al.*, 2007; *Yu and Hickey*, 2007; *Snively and Pasko*, 2008; *Huang et al.*, 2010; *Heale and Snively*, 2015]. It was found that waves trapped in ducts can propagate large horizontal distances, depositing their energy and momentum periodically as they leak from the duct [*Heale et al.*, 2014a; *Suzuki et al.*, 2013b]. In addition, it was found that the inclusion of time-dependent background winds can lead to a reduction in filtering, as critical levels now become transient [*Broutman and Young*, 1986; *Eckermann*, 1997; *Sartelet*, 2003; *Vanderhoff et al.*, 2008]. *Heale and Snively* [2015] also found that reflection of a wave can be reduced once the time dependence of a background wind is considered. Both cases lead to additional upward propagation over time-independent background assumptions.

In this study, we use simultaneous data from collocated sodium lidar and airglow imager on 16 January 2015 at Andes Lidar Observatory (ALO) to depict a GW event in 3-D space. Thus, the horizontal and vertical structures of wave packet and its ambient atmosphere states are fully characterized. This observation is unique in that it provides a clear case of both wave reflection and critical level filtering. A numerical simulation is performed with the observed wave parameters using a fully compressible, nonlinear 2-D numerical model, which shows that double reflection leads to a leaky duct and a near-critical level occurs when wave speed approaches background wind speed. The simulation yields a comparison and a confirmation of our interpretation of observations. The paper is organized as follows: Section 2 describes the instrumentation, data set, and numerical model. Section 3 presents the observational results from the sodium lidar and airglow imager. Section 4 discusses the numerical model setup and simulation results. Finally, the summary and conclusions are presented in section 5.

2. Instruments and Numerical Model

2.1. Sodium Lidar

A narrow-band sodium temperature/wind lidar system is a powerful active remote sensing instrument that can measure the atmospheric temperature, neutral winds, and sodium density from 80 to 105 km altitude [*Gardner and Papen*, 1995]. The University of Illinois at Urbana-Champaign (UIUC) lidar system was deployed in ALO at Cerro Pachón (30.25°S, 70.73°W), Chile, since September 2009. The lidar is equipped with four telescopes each of 75 cm diameter, which are fixed at zenith direction, and 20° off zenith toward the south, west, and east directions. The laser beam is tuned to the sodium D2a line at 589 nm and pointed to the four directions alternately, and the return photons are collected by the corresponding telescope. Sodium density, temperature, and line-of-sight winds along the laser beam are derived from return signals. The line-of-sight winds are converted to horizontal (zonal and meridional) winds based on the off-zenith angle [*Krueger et al.*, 2015]. The typical temporal resolution of the measurements is 90 s, and spatial resolution is 500 m. At this resolution, the measurement accuracies are ~1 K for temperature and ~0.5 m s^{-1} for vertical winds near peak sodium density altitudes. On the night of 16 January 2015, the laser beam was only pointed to the zenith;

therefore, only vertical winds were acquired. On later nights, the lidar was operated in normal mode and both horizontal and vertical winds were obtained.

2.2. Airglow Imager

Airglow refers to the emission of photons in the upper atmosphere via chemiluminescence processes, that mainly result from reaction with atmospheric species such as atomic oxygen and hydroxyl radicals. Variations in airglow intensity can be used to infer GW properties [*Molina*, 1983; *Taylor*, 1997; *Nappo*, 2012, and references therein] as the waves interact with the photochemistry. An all-sky airglow imager was installed and operated in the same observatory as the lidar. The imager is equipped with two filters and captured hydroxyl (OH) emission near ~87 km and atomic oxygen (OI) emission near ~96 km alternately at night during the low moon period throughout the year. The airglow emissions were collected by a 1024 × 1024 CCD array and then binned to a 512 × 512 array to increase signal-to-noise ratio. The integration times for the OH and OI images are 1 min and 1.5 min, respectively. High-frequency, quasi-monochromatic GWs are identified from the images using a series of procedures described in detail in *Tang et al.* [2002, 2005a, 2005b]. These GWs typically have horizontal wavelengths of several tens of kilometers, vertical wavelengths longer than 10 km, and periods of 5–20 min [*Li et al.*, 2012].

2.3. Numerical Model

A nonlinear, fully compressible, two-dimensional numerical model, developed by *Snively and Pasko* [2008] and updated by *Snively et al.* [2013], is used to simulate the observed GW processes. The model solves the nonlinear and compressible Euler equations using an adaptation of the Clawpack routines *LeVeque* [2002] for hyperbolic systems of equations. The model solves a Riemann problem at each cell interface by calculating individual characteristic waves and characteristic speeds. These waves are then propagated at each time step and summed up to calculate the flux passing across each cell boundary using a finite volume approach. Dissipation through molecular viscosity and thermal conductivity is solved separately using a time split method. The same model has been used extensively to investigate the propagation, dissipation, and interaction of GWs in the MLT region [*Snively et al.*, 2007; *Heale et al.*, 2014a, 2014b; *Heale and Snively*, 2015; *Yuan et al.*, 2016].

3. Observational Results

3.1. Lidar Measurements

Raw lidar measurements smoothed by a 15 min moving average are shown in Figure 1, the perturbation of the vertical wind exceeds ±10 m s^{-1} at certain altitudes. Distinct wave patterns with a period of about a half hour can be identified in the temperature and vertical wind measurements. In order to obtain the dominant periods of the waves, Fourier analysis was applied to the raw lidar data with a 90 s resolution at all altitudes. Several peaks around ~30 min were identified in the spectra of temperature and vertical wind. A Chebyshev type II band-pass filter was used to extract the waves from the raw measurements with an 18 min lower 3 dB cutoff period and a 35 min upper 3 dB cutoff period. The background temperature $\overline{T}$ was obtained using another low-pass filter with a cutoff period of 40 min. Squared buoyancy frequency N^2 is calculated as

$$N^2 = \frac{g}{\overline{T}}\left(\frac{\partial \overline{T}}{\partial z} + \frac{g}{c_p}\right), \tag{1}$$

where g is the gravity acceleration and c_p is the specific heat at constant pressure. Larger values of N^2 indicate more stable atmosphere, while values of negative N^2 imply a statically unstable atmosphere. The squared buoyancy frequencies N^2 shown in Figure 2 reveal that the background atmosphere is mostly stable, but layers with relatively smaller values of N^2 can be found near 92 km and 98 km.

The resulting band-pass filtered temperature and vertical winds are shown in Figure 3. Perturbations of vertical wind have a lag about 90° with respect to temperature, which matches the polarization relation of GWs. Both variables show clear layered structure. In the temperature perturbations, three layers exist: one is below 92 km, the second is centered at 95 km with thickness of ~2 km, and the third one is above 98 km. In the vertical wind perturbations, only two layers exist and mostly match the temperature perturbation except that the perturbations are minimized near 95 km. For the layer below 92 km, the phase of temperature and vertical wind perturbations are almost vertically oriented and the amplitudes of the waves exceed 15 K and

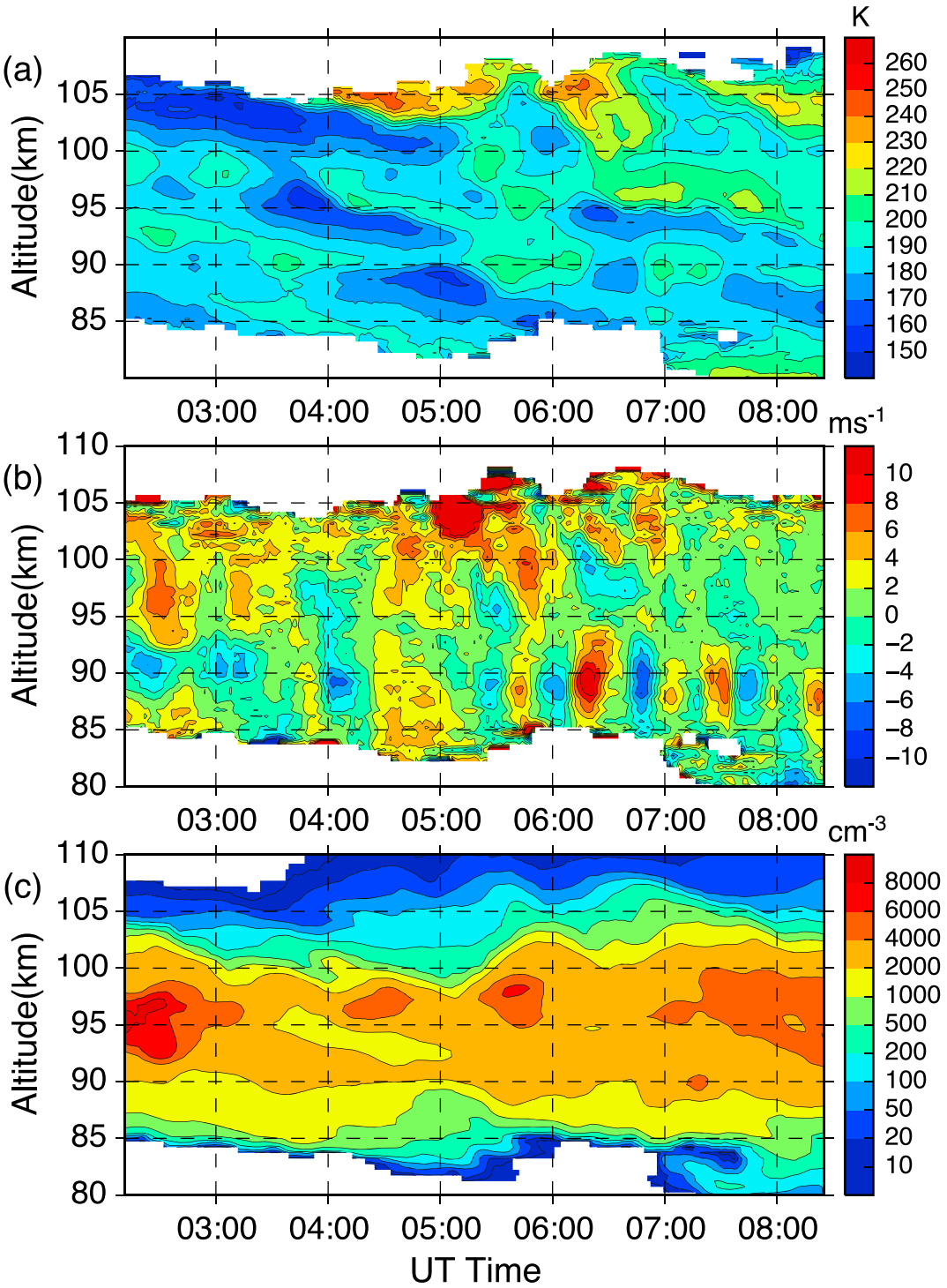

Figure 1. The smoothed raw lidar (a) temperature, (b) vertical wind, and (c) sodium density on the night of 16 January 2015.

10 m s^{-1}. Smaller values of N^2 ($\leq 2\times10^{-4}$ s^{-2}) are also denoted by solid contour lines in Figure 3a. Although the atmosphere is found to be mostly stable, there still exist a few layers relatively unstable that would not be favorable for GW propagation. The layered structures of wave patterns are related to the atmospheric stability, with the temperature perturbation maxima corresponding to regions of larger N^2 (i.e., stable regions). More detailed discussions can be found in later sections about simulation results.

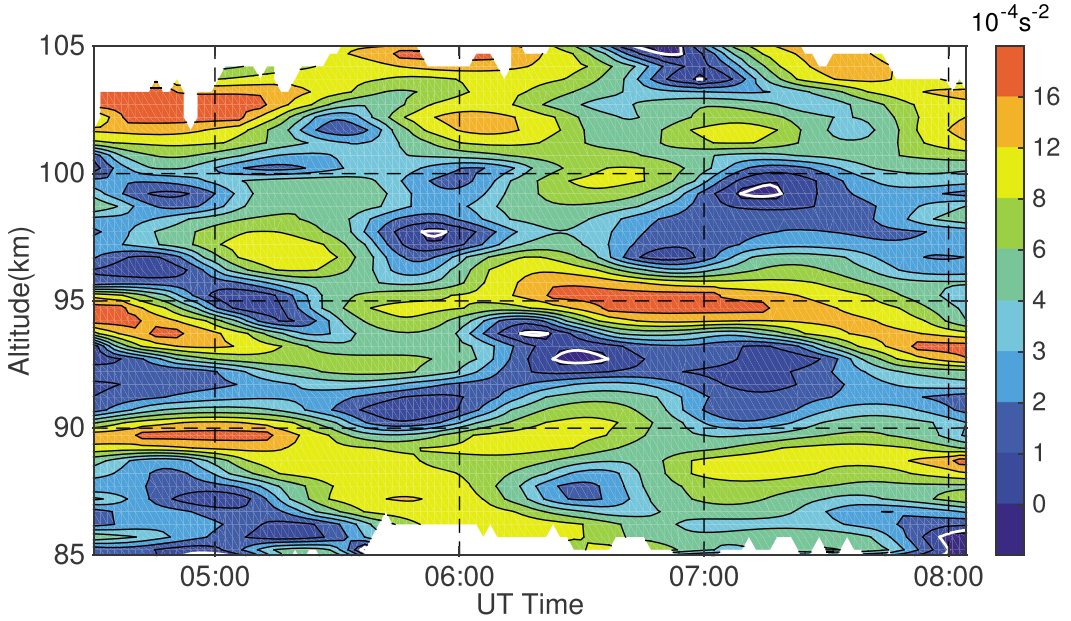

Figure 2. The squared buoyancy frequencies calculated from background temperature. Zero contours are highlighted with thick white lines.

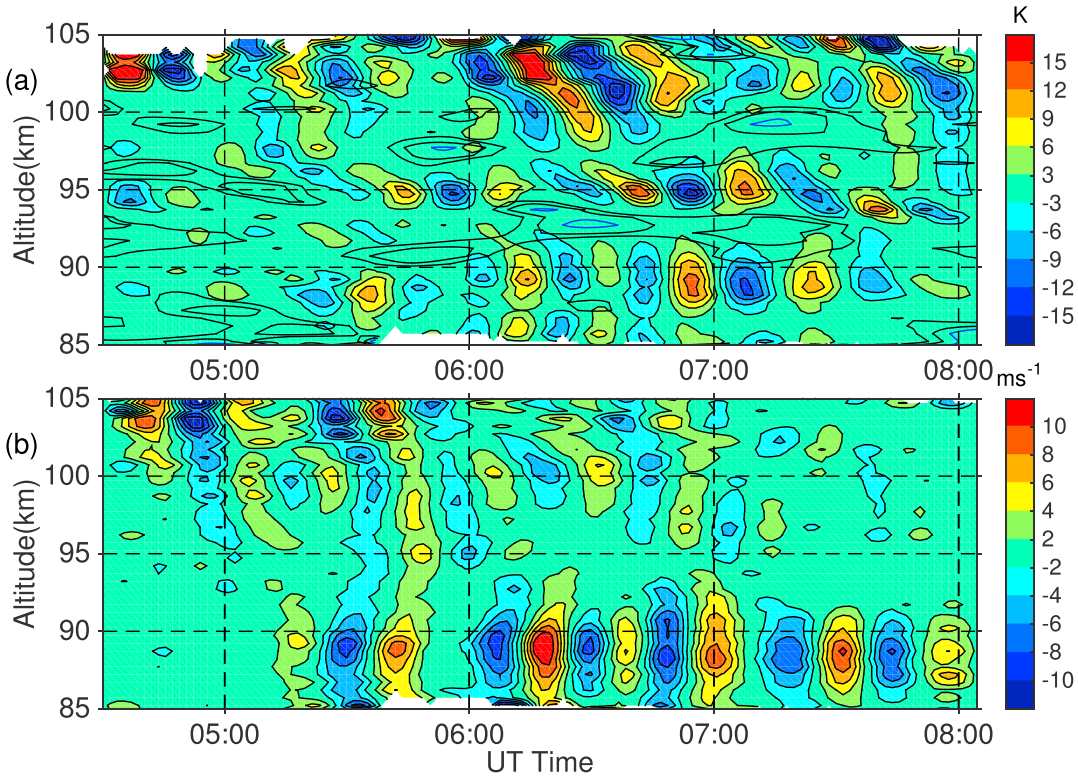

Figure 3. The band-pass filtered lidar (a) temperature and (b) vertical wind perturbations. The smaller values of N^2 (0, 1×10^{-4} s^{-2}, 2×10^{-4} s^{-2}) are shown by contours in temperature perturbation.

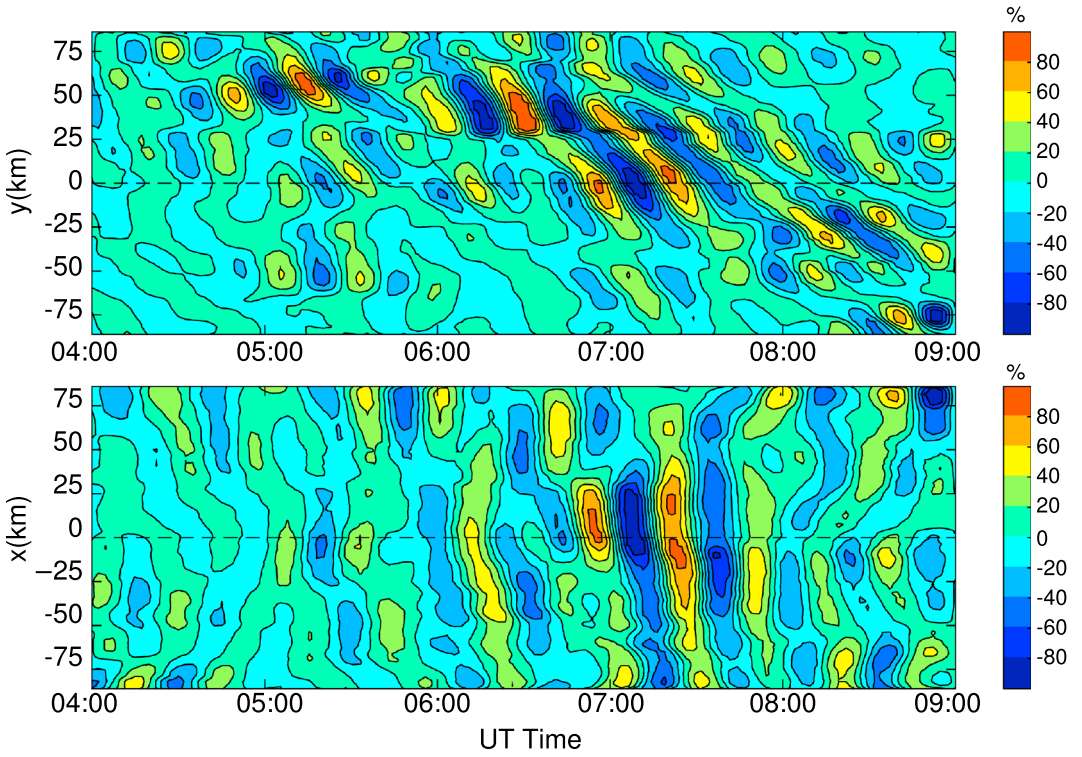

Figure 4. The keograms of OH airglow emission intensity in (top) north-south direction and (bottom) east-west direction. The positive distance is to the north and east of the ALO. The color scale is the normlized airglow emission intensity in percentage.

3.2. Airglow Images

OH airglow images were preprocessed by standard procedures including star removal, coordinate unwrapping, and Milky Way removal. Only image pixels within ±45° off zenith were processed due to their higher resolution (≤1 km/pixel). The preprocessed images cover a square area of 172 km in each direction. Firstly, the same band-pass filter that was used in processing the lidar data was applied on the airglow intensity for each image pixel in time domain. Then, a 2-D median filter was used to suppress the noisy and small structures in each image.

In order to demonstrate the temporal evolution of the GW packet in the airglow images, one column and one row of image pixels, which includes the zenith pixel, were extracted from the preprocessed images to make "keograms," i.e., the distance-versus-time plots of airglow intensity. Note that the unit here is normalized airglow emission intensity in percentage. In Figure 4, the wave pattern is present and strong from 5:00 UT onward, matching the lidar measurements near ~87 km in Figure 3. A clear phase tilt is found in the north-south direction but not in the east-west direction. This implies that the GW packet propagates mostly southward. Figure 5 shows four consecutive airglow images with an interval of 5 min and note that the center area of each image corresponds to the zenith-pointing direction of lidar. The wave pattern is distinct in the airglow images and propagate mostly southward. Finally, the horizontal wavelength and propagation direction of dominant wave were calculated based on a 2-D spectral analysis.

By combining measurements from lidar and airglow imager, all parameters of this GW packet are determined and listed in Table 1. It is assumed that these parameters do not vary too much within the observation time and altitude range. We chose the wave period to be 27 min for the simulation because it is the most dominant period as revealed by the spectral analysis.

4. Numerical Simulation

4.1. Model Setup

The simulation domain is set to be 600 km in the horizontal (*x* direction) and 170 km in the vertical (*z* direction), with a resolution of 2 km in horizontal and 0.25 km in vertical. The side and top boundaries are open, and

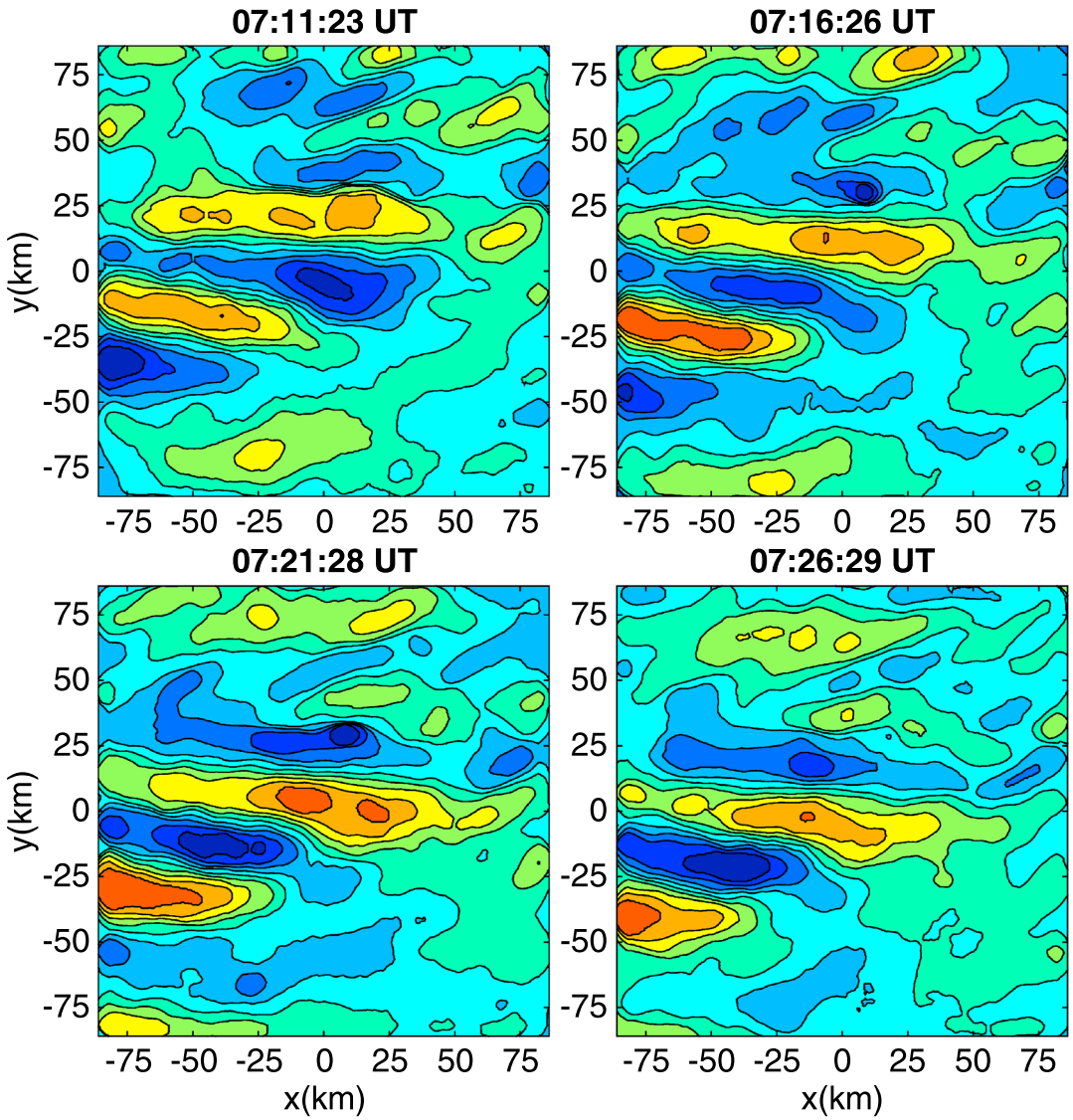

Figure 5. Four consecutive temporally filtered and spatially smoothed airglow images with a 5 min interval. The *x* and *y* distances are in east-west and north-south directions. Same color scale as Figure 4 is used.

the bottom boundary (ground) is set to be closed (reflective). The simulation outputs result every 90 s, to be consistent with the lidar measurements, and the simulation runs for ~6 h. The GW packet is generated by a spectrally coherent, idealized vertical body forcing applied below the observable altitudes and specified by a Gaussian modulated cosine wave, which has been used frequently in numerical simulation

$$F_z(x,z,t) = A \cdot \exp\left[-\frac{(x-x_c)^2}{2\sigma_x^2} - \frac{(z-z_c)^2}{2\sigma_z^2} - \frac{(t-t_c)^2}{2\sigma_t^2}\right] \cdot \cos\left[\omega(t-t_c) - k(x-x_c)\right] \quad (2)$$

The source location is set at x_c = 200 km and z_c = 65 km (to reduce computational time) and t_c = 108 min. The scale of wave is set to $k = 2\pi/50$ km^{-1}, $\omega = 2\pi/27$ min^{-1}, which are all determined from observations as listed in Table 1. The parameters σ_x, σ_z, and σ_t are 200 km, 65 km, and 27 min, respectively. The amplitude A is chosen to be 0.12 m s^{-1}, which corresponds to a source amplitude of 0.002 m s^{-1} at tropopause. This amplitude is determined tentatively to match simulation results with those seen in the observations without visible wave breaking, which could diminish the wave amplitudes.

Table 1. The Wave Parameters Identified From Lidar and Airglow Imager

Variables	Values
Date, time	2015/1/16, 04:30–08:10 UT
Period	27 (18–35) min
Horizontal wavelength	50 km
Horizontal wave Speed	30 m s^{-1}
Propagation direction[a]	190°
Wave amplitudes	~15 K in T', ~10 m s^{-1} in w'

[a]The direction is measured clockwise from north.

For the numerical simulation, the background condition is very important. The background temperature profile is determined using an average of the lidar temperature between 05:00 UT and 08:00 UT merged with temperature from NRLMSISE-00 [*Picone et al.*, 2002] set to the same location and time. Due to the lidar being operated in zenith mode only, horizontal winds were not available until 26 January 2015. However, the horizontal winds of the following nights show some long-term consistency. Thus, the background horizontal wind used for the simulation is an amalgamation of the HWM-07 winds [*Drob et al.*, 2008] of the same time period and the averaged lidar winds from 26 January to 2 February.

In linear GW theory, the dispersion relation is used to diagnose the propagation of GWs and potential reflection and critical layers. Equation (3) is a complete analytical expression of the dispersion relation based on Taylor-Goldstein equation [*Nappo*, 2012], including the vertical wind shear and curvature terms.

$$m^2 = \frac{N^2}{(c-u_0)^2} + \frac{1}{c-u_0}\frac{\mathrm{d}^2u_0}{\mathrm{d}z^2} - \frac{1}{H(c-u_0)}\frac{\mathrm{d}u_0}{\mathrm{d}z} - k^2 - \frac{1}{4H^2} \tag{3}$$

Through this equation, the vertical wave number m is related to the wave phase speed c, the background winds u_0, the horizontal wave number k, and the scale height H. In the regions of atmosphere where $m^2 > 0$, GWs are able to propagate freely and are characterized by corresponding m, k, and c. Regions of $m^2 < 0$ indicate evanescence for GWs, whose amplitudes will decay exponentially. When a propagating wave encounters

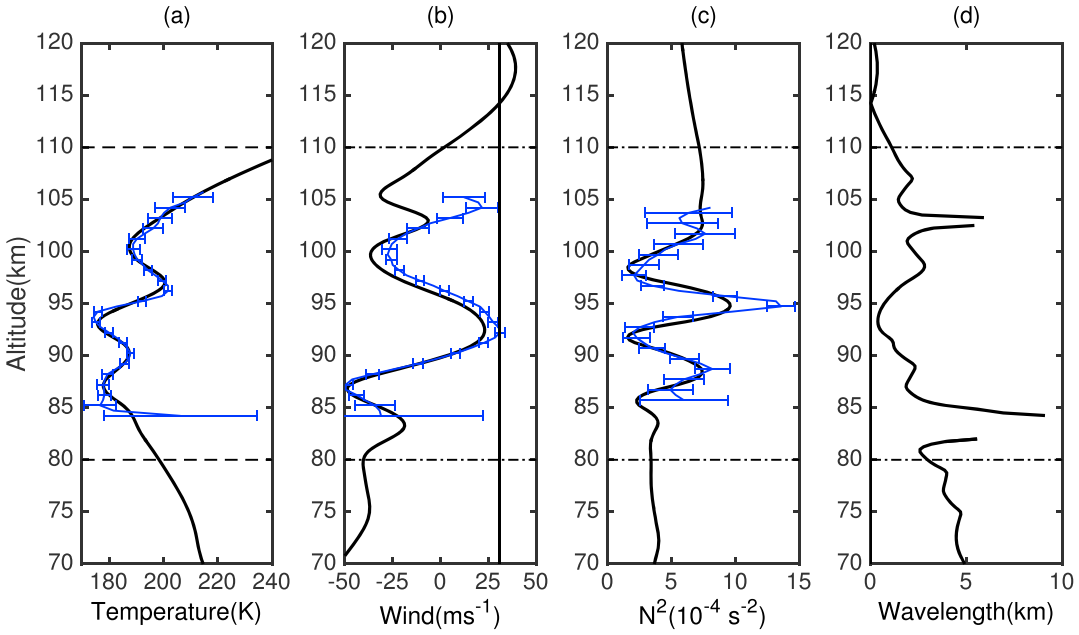

Figure 6. The background (a) temperature, (b) horizontal wind, (c) calculated squared buoyancy frequency, and (d) calculated vertical wavelength. Blue lines with error bars are observations or calculated directly from observations, and black lines are models data merged with observations. Two horizontal dash-dotted lines mark the approximate observational altitude range.

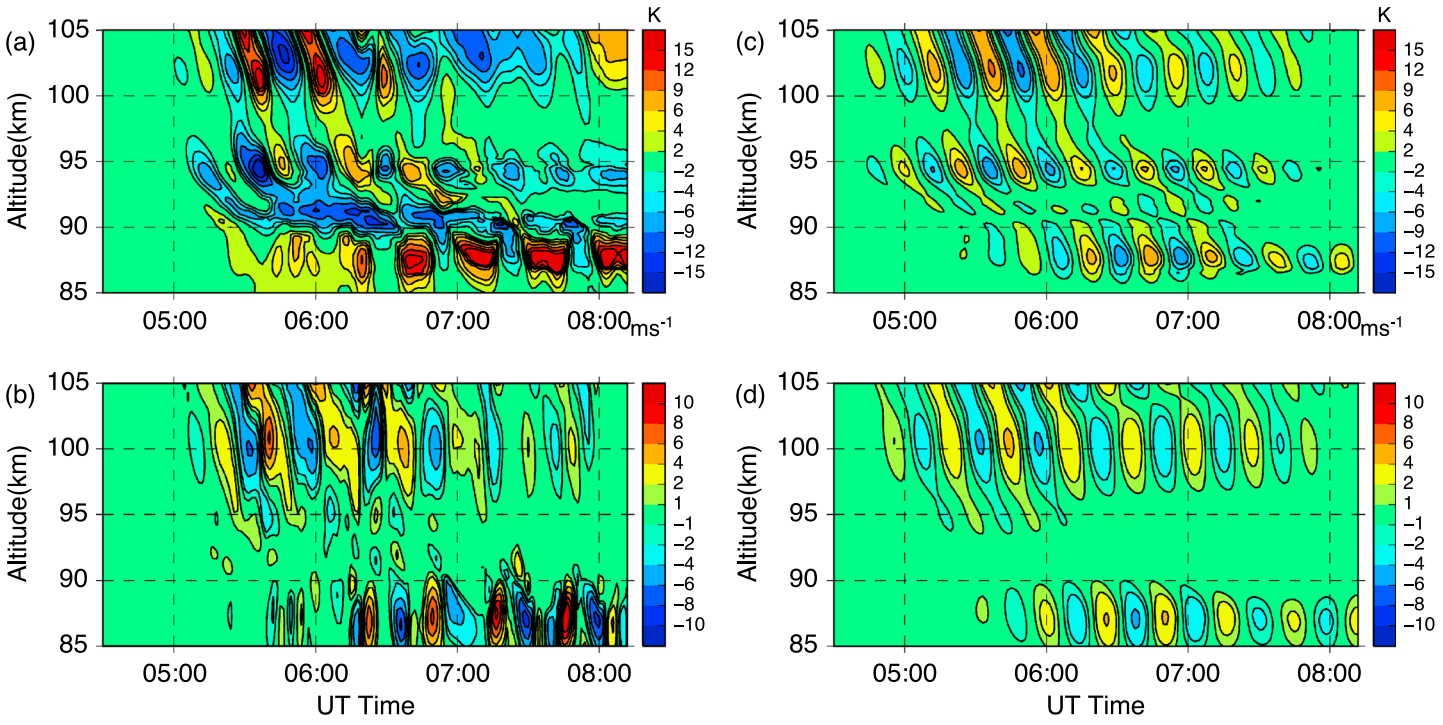

Figure 7. The (a) original and (c) filtered temperature perturbation, and (b) original and (d) filtered vertical wind perturbation at virtual lidar site (x = 340 km) in simulation domain.

a region where $m^2 < 0$, partial or total reflection can occur depending on the depth of the evanescent region. At altitudes where $c = u_0$, a wave can be partially or completely critical layer filtered as the vertical wave number approaches infinity and breaking or dissipation occurs.

Figures 6a–6c show the background temperature, horizontal wind projected along the wave propagation direction, and squared buoyancy frequency, respectively. Lines in blue show the observations with errors, and lines in black show the merged profiles of observations and empirical models, which are used for the simulations. Using equation (3), the vertical wave number m can be calculated from all the wave and background parameters. The vertical wavelength is then obtained as $\lambda_z = 2\pi/\mathrm{m}$ for all positive m^2 and shown in Figure 6d. Two reflection layers are found, corresponding to negative m^2 and denoted by the two broken parts on the curve. One reflection layer is below 85 km, and the other is around 103 km. At ~92 km altitude, the wave phase speed approaches the background wind speed, leading to a near-critical layer. At this altitude, the vertical wavelength becomes very small, and the wave phase fronts will be oriented almost horizontally, leading to greater tendency toward large shears and thus instability.

4.2. Simulation Results

Due to simplifications in the physics of the simulation, i.e., imposing a time-independent constant background and quasi-monochromatic waves, which may not represent the full spectrum, differences between observations and simulations are expected. However, the simulation captures and helps to explain the major features while illustrating the spatial evolution of the wave fields.

As GW packets propagate away from their sources, they will be dispersed, refracted, and filtered by the background atmosphere, spreading and depositing the energy and momentum of the packet throughout the atmosphere. Therefore, an instrument at a fixed location relative to the wave source may only capture part of the wave spectrum as a wave passes through the instrument's field of view. When simulations are compared with lidar observations from a single site, it is important to pick a "virtual lidar" location within the model domain to transform an x-z domain into a t-z domain. Following the analysis method applied in *Yuan et al.* [2016], we tested several virtual lidar sites and found that results at x = 340 km (140 km away from the specified source horizontally) best match the observations and are thus selected to compare with observations in later analyses.

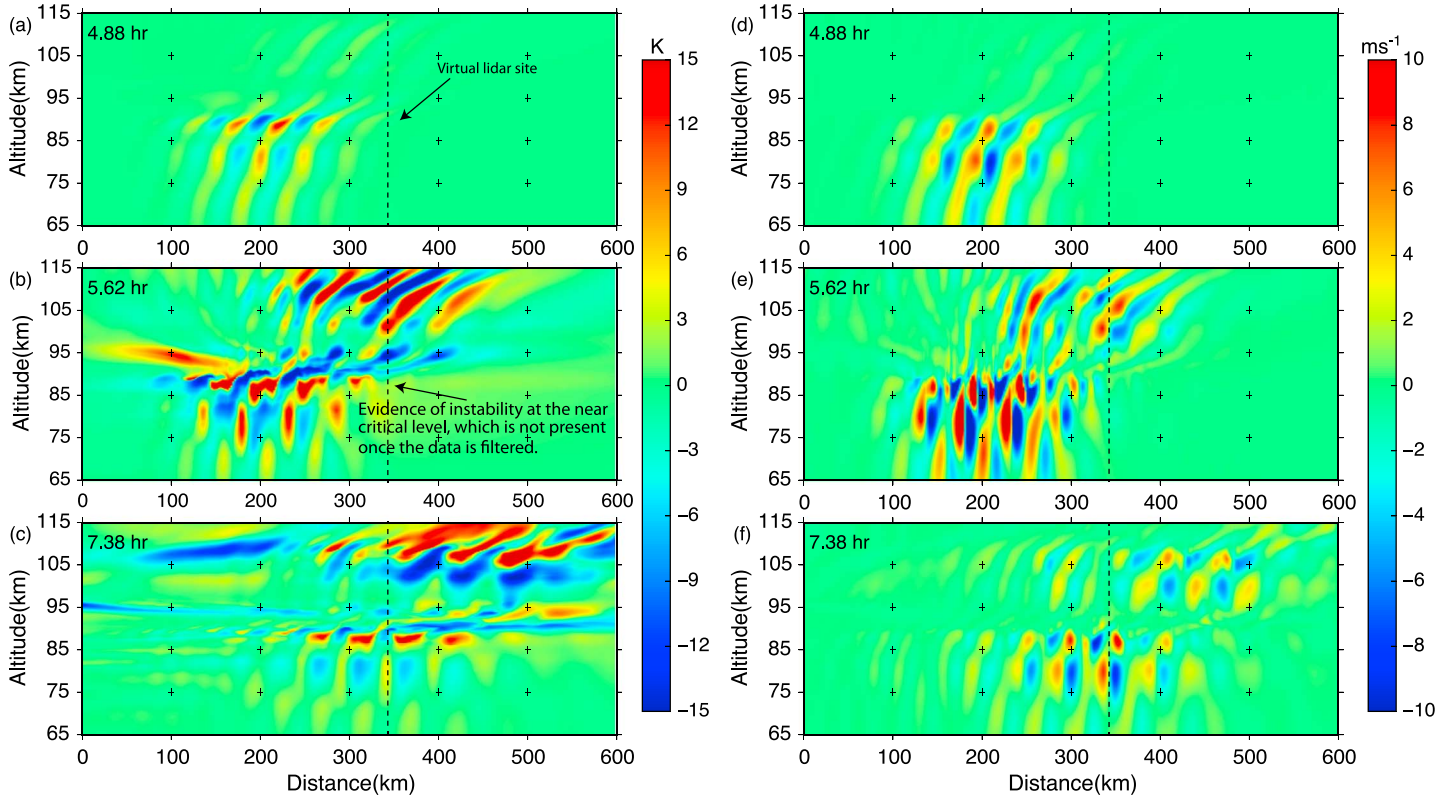

Figure 8. The original simulated (a–c) temperature and (d–f) vertical wind perturbations at t = 4.88, 5.62, and 7.38 h. Please note that the virtual lidar site is at x = 340 km and denoted by the vertical dashed line.

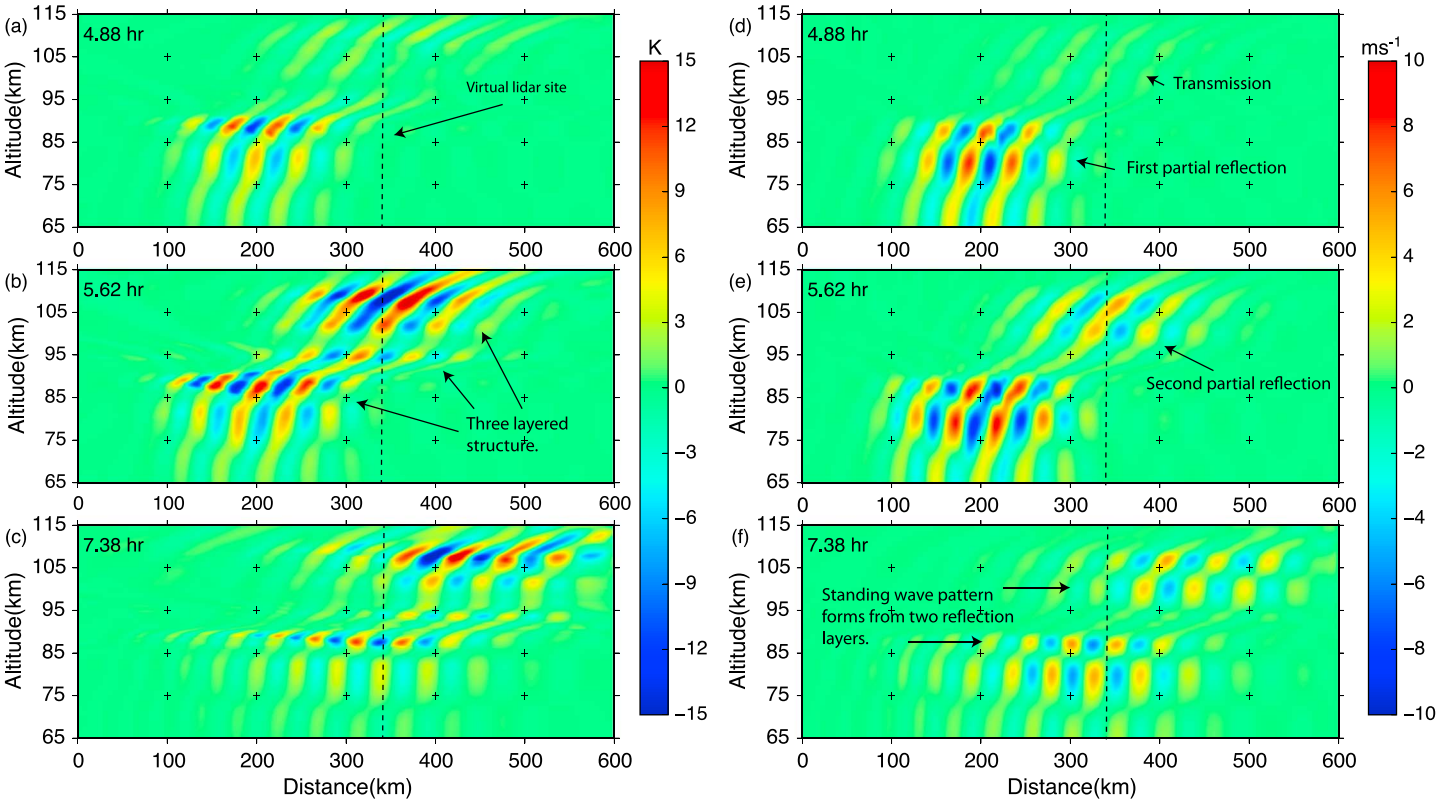

Figure 9. The filtered simulated (a–c) temperature and (d–f) vertical wind perturbations at t = 4.88, 5.62, and 7.38 h.

Figures 7a and 7c (7b and 7d) depict the original and filtered temperature (vertical wind) perturbations from the virtual lidar site. The filtering is done using the same filter as the one used in the lidar and airglow measurements. For easier comparison, the time of numerical simulation is adjusted to match the observation time and also called UT time, since the simulation time is arbitrary. A propagating GW packet is generated when the source is active from approximately 4.75 to 5.65 h (adjusted by adding 3.4 h from the t in equation (2)). Layered structures are found at similar altitudes to the observations. The amplitudes of temperature and vertical wind perturbations reach maximums of ± 10 K and ± 6 m s^{-1}, respectively. The model-simulated amplitudes are slightly smaller because only part of spectrum was simulated. In Figures 7a and 7c, there is a thin layer right above 90 km with strong and constant negative temperature perturbations and without obvious vertical wind perturbations corresponding to a near-critical layer. It is also in part the result of wave packet dispersion. The three-layered enhancements (87 km, 95 km, and 103 km) in the temperature perturbations correspond to stable regions of relatively large N^2. Figure 7d shows strong enhancements in vertical wind at ~87 km and ~101 km, corresponding to reflection levels as indicated in Figure 6d. This is because the wave phase fronts will orientate themselves more vertically as the vertical wavelength increases. Near 95 km above the near-critical layer, the atmosphere is stable and temperature perturbations are strong. However, only weak vertical wind perturbations are found there. This is due to the fact that wave fronts tend to be oriented horizontally, reducing their contribution to the vertical winds. It is also important to note that the reflection appears at 101 km before it does at 87 km, suggesting that the wave reflection at 87 km is, in part, a second reflection from the downward propagating portion of the wave packet that was reflected at 101 km.

In order to demonstrate the dynamics of the wave propagation, we select three frames from the x-z domain of simulation results at $t = 4.88$ h, 5.62 h, and 7.38 h for both temperature and vertical wind. The original frames are shown in Figure 8, and the filtered frames are shown in Figure 9. At 4.88 h, a small portion of the wave packet has penetrated the evanescent region near 85 km and continued to propagate upward. We can see that the main energy center of the wave packet has not yet reached the $x = 340$ km virtual lidar site and is beginning to be reflected at ~85 km altitude between $x = 100$ and 300 km.

About 45 min later at $t = 5.62$ h, the wave packet is partially reflected at both 85 km and 101 km, and the energy of the wave is split between the upper and lower reflection levels. The portion of the wave packet at 85 km altitude has still not propagated far enough horizontally to enter the field of view of the virtual lidar, and a considerable amount of the wave energy has already been reflected and will not be observable at the virtual lidar site. This shows the huge dependance of the relative distance between the instrument site and the source, which determines the components of wave spectrum or portion of wave processes that are actually observed.

At $t = 7.38$ h, we see a clear standing wave type pattern (especially in the filtered cases in Figure 9) in the vertical wind at both 85 km and 101 km indicative of strong reflection at both layers and ducting within. While it is not clear from a single frame, the wave at 85 km is in fact the result of reflection from 101 km at earlier times as well as some transmission of the upgoing waves. Also, note the horizontal dispersion of the wave packet which now spans $x \sim 100$–500 km. Finally, the bottom portion of the wave packet becomes visible at the $x = 340$ km virtual lidar site.

5. Summary and Conclusions

The details of GW reflection and critical level are seldom observed in the atmosphere. Even when they are, the processes are not easy to understand due to incomplete measurements or spatial/temporal coverage of all physical quantities involved. And most numerical simulations are limited in artificially selected parameters. In this study, the combination of two different data sets reveals a unique and distinct GW packet event that undergoes partial reflection at two altitudes and approaches a near-critical layer in between. We have conducted a detailed and comprehensive investigation of this event. The GW packet was determined with a ground-based period about 18–35 min, a horizontal wavelength ~50 km, and nearly southward propagation direction. The event was also successfully modeled by a mesoscale numerical model, which captures primary features in the observations and provides an opportunity to understand the dynamical processes outside of the limited field of view of the instrumentation.

The observations show a three-layered structure (peak amplitudes at 90 km, 95 km, and 103 km) in the temperature perturbations and a two-layered structure in the vertical winds (peaks at 87 km and 101 km)

with amplitudes exceeding 15 K and 10 m s^{-1}, respectively, and minima in between these layers. The three-layered structure in temperature corresponds to regions of relatively large N^2 regions (stable regions), and the two-layered structure in vertical wind corresponds to reflection levels which shift the wave to large vertical scales and subsequently large amplitudes. The numerical model predicts the layered structure and approximate amplitude, although only part of the spectra was simulated so that amplitudes are slightly underestimated. The model suggests that the wave packet undergoes dual reflection and transmission at ~85 km and 101 km altitude and that the portion of the wave seen at later times at lower altitudes is in part the result of reflection and downward propagation of the wave from the upper altitudes. Due to the cancelation effects of GWs in airglow layer [*Liu and Swenson*, 2003], waves of vertical wavelength around 3 km should be barely visible in the airglow imager. However, the wave reflection enables the waves to be captured by an airglow imager. The model also suggests that the near-critical layer at ~93 km altitude leads to enhanced shears and thus instability in the wave field. Notably, these features are not clearly apparent when viewing filtered data. The model results reveal the capture of waves within a duct under realistic condition. The dispersion of the wave packet by reflection and near-critical levels was clearly observed, here providing insight into the evolution of GW packet at small scales. The model results highlight that the location of the instrument relative to the source can determine the portion of the wave spectrum and processes that are observed by the instrument.

This study demonstrates how a combination of instrumentation and modeling can be used to supplement each other to provide a greater explanation of GW events. To consider the effects of GWs, it is important to understand how GWs interact with the background atmosphere through reflection and critical levels. The detailed calculation and analysis of heat and momentum flux around these levels from observations and simulations are prospective work in the future.

Acknowledgments
The data and program used in this analysis can be obtained upon request (caob@my.erau.edu). The ALO sodium lidar and airglow imager data are also available at http://lidar.erau.edu. This work is supported by NSF grants AGS-1110199 and AGS-1115249 and NSFC grant 41274154. Research by C.J. Heale and J.B. Snively is supported under NSF grant AGS-1344356 and using models developed under AGS-1151746. The lidar operation at ALO was partially supported by NSF grant AGS-1229085. The ALO is part of the Consortium of Resonance and Rayleigh Lidars, supported by NSF grants AGS-1136278 and AGS-1136208. We are grateful for the excellent support of the ALO facility provided by the Association of Universities for Research in Astronomy (AURA).

References

Andrews, D. G., J. R. Holton, and C. B. Leovy (1987), *Middle Atmosphere Dynamics*, 40, Academic Press, New York.

Bossert, K., D. C. Fritts, P. D. Pautet, M. J. Taylor, B. P. Williams, and W. R. Pendleton (2014), Investigation of a mesospheric gravity wave ducting event using coordinated sodium lidar and Mesospheric Temperature Mapper measurements at ALOMAR, Norway (69°N), *J. Geophys. Res. Atmos.*, *119*, 9765–9778, doi:10.1002/2014JD021460.

Broutman, D., and W. Young (1986), On the interaction of small-scale oceanic internal waves with near-inertial waves, *J. Fluid. Mech.*, *166*, 341–358.

Cai, X., T. Yuan, Y. Zhao, P.-D. Pautet, M. J. Taylor, and W. R. Pendleton (2014), A coordinated investigation of the gravity wave breaking and the associated dynamical instability by a Na lidar and an Advanced Mesosphere Temperature Mapper over Logan, UT (41.7°N, 111.8°W), *J. Geophys. Res. Space Physics*, *119*, 6852–6864, doi:10.1002/2014JA020131.

Chen, C., X. Chu, A. J. mcDonald, S. L. Vadas, Z. Yu, W. Fong, and X. Lu (2013), Inertia-gravity waves in Antarctica: A case study using simultaneous lidar and radar measurements at McMurdo/Scott Base (77.8°S, 166.7°E), *J. Geophys. Res. Atmos.*, *118*, 2794–2808, doi:10.1002/jgrd.50318.

Chen, C., X. Chu, J. Zhao, B. R. Roberts, Z. Yu, W. Fong, X. Lu, and J. A. Smith (2016), Lidar observations of persistent gravity waves with periods of 3–10 h in the Antarctic middle and upper atmosphere at McMurdo (77.83°S, 166.67°E), *J. Geophys. Res. Space Physics*, *121*, 1483–1502, doi:10.1002/2015JA022127.

Cohen, N. Y., E. P. Gerber, and O. Bühler (2014), What drives the Brewer–Dobson Circulation?, *J. Atmos. Sci.*, *71*(10), 3837–3855, doi:10.1175/JAS-D-14-0021.1.

Drob, D. P., et al. (2008), An empirical model of the Earth's horizontal wind fields: HWM07, *J. Geophys. Res.*, *113*, A12304, doi:10.1029/2008JA013668.

Dunkerton, T. J., and D. C. Fritts (1984), Transient gravity-wave critical layer interaction. Part I: Convective adjustment and the mean zonal acceleration, *J. Atmos. Sci.*, *41*(6), 992–1007, doi:10.1175/1520-0469(1984)041<0992:TGWCLI>2.0.CO;2.

Eckermann, S. D. (1997), Influence of wave propagation on the Doppler spreading of atmospheric gravity waves, *J. Atmos. Sci.*, *54*(54), 2554–2573.

Espy, P. J., R. E. Hibbins, G. R. Swenson, J. Tang, M. J. Taylor, and D. M. Riggin (2006), Regional variations of mesospheric gravity-wave momentum flux over Antarctica, *Ann. Geophys.*, *24*(1), 81–88, doi:10.5194/angeo-24-81-2006.

Franke, P. M., and W. A. Robinson (1999), Nonlinear behavior in the propagation of atmospheric gravity waves, *J. Atmos. Sci.*, *56*(17), 3010–3027, doi:10.1175/1520-0469(1999)056.

Fritts, D. C. (1984), Gravity wave saturation in the middle atmosphere: A review of theory and observations, *Rev. Geophys. Space Phys.*, *22*, 275–308.

Fritts, D. C., and M. J. Alexander (2003), Gravity wave dynamics and effects in the middle atmosphere, *Rev. Geophys.*, *41*(1), 1003, doi:10.1029/2001RG000106.

Fritts, D. C., and T. S. Lund (2011), *Gravity Wave Influences in the Thermosphere and Ionosphere: Observations and Recent Modeling Aeronomy of the Earth's Atmosphere and Ionosphere*, pp. 109–130, Springer, Dordrecht, Netherlands.

Fritts, D. C., and P. K. Rastogi (1985), Convective and dynamical instabilities due to gravity wave motions in the lower and middle atmosphere: Theory and observations, *Radio Sci.*, *20*(6), 1247–1277.

Fritts, D. C., L. Wang, and J. A. Werne (2013), Gravity wave-fine structure interactions. Part I: Influences of fine structure form and orientation on flow evolution and instability, *J. Atmos. Sci.*, *70*(12), 3710–3734, doi:10.1175/JAS-D-13-055.1.

Fritts, D. C., P.-D. Pautet, K. Bossert, M. J. Taylor, B. P. Williams, H. Iimura, T. Yuan, N. J. Mitchell, and G. Stober (2014), Quantifying gravity wave momentum fluxes with Mesosphere Temperature Mappers and correlative instrumentation, *J. Geophys. Res. Atmos.*, *119*, 13,583–13,603, doi:10.1002/2014JD022150.

Gardner, C. S., and G. C. Papen (1995), Mesospheric Na wind/temperature lidar, *Laser Rev.*, *23*(2), 131–134.

Gierasch, P., R. Goody, and P. Stone (1970), The energy balance of planetary atmospheres, *Geophys. Fluid Dyn.*, *1*, 1–18.
Heale, C. J., and J. B. Snively (2015), Gravity wave propagation through a vertically and horizontally inhomogeneous background wind, *J. Geophys. Res. Atmos.*, *120*, 5931–5950, doi:10.1002/2015JD023505.
Heale, C. J., J. B. Snively, and M. P. Hickey (2014a), Numerical simulation of the long-range propagation of gravity wave packets at high latitudes, *J. Geophys. Res. Atmos.*, *119*, 11,116–11,134, doi:10.1002/2014JD022099.
Heale, C. J., J. B. Snively, m. P. Hickey, and C. J. Ali (2014b), Thermospheric dissipation of upward propagating gravity wave packets, *J. Geophys. Res. Space Physics*, *119*, 3857–3872, doi:10.1002/2013JA019387.
Hecht, J. H., R. L. Walterscheid, D. C. Fritts, J. R. Isler, D. C. Senft, C. S. Gardner, and S. J. Franke (1997), Wave breaking signatures in OH airglow and sodium densities and temperatures 1. Airglow imaging, Na lidar and MF radar observations, *J. Geophys. Res.*, *102*(D6), 6655–6668.
Holton, J. R., P. H. Haynes, m. E. mcIntyre, A. R. Douglass, R. B. Rood, and L. Pfister (1995), Stratosphere-troposphere exchange, *Rev. Geophys.*, *33*(4), 403–439, doi:10.1029/95RG02097.
Hu, X., A. Z. Liu, C. S. Gardner, and G. R. Swenson (2002), Characteristics of quasi-monochromatic gravity waves observed with lidar in the mesopause region at Starfire Optical Range, NM, *Geophys. Res. Lett.*, *29*(24), 2169, doi:10.1029/2002GL014.975.
Huang, K. M., S. D. Zhang, and F. Yi (2010), Reflection and transmission of atmospheric gravity waves in a stably sheared horizontal wind field, *J. Geophys. Res.*, *115*, D16103, doi:10.1029/2009JD012687.
Huang, K. M., A. Z. Liu, S. D. Zhang, F. Yi, and Z. Li (2012), Spectral energy transfer of atmospheric gravity waves through sum and difference nonlinear interactions, *Ann. Geophys.*, *30*(2), 303–315.
Krueger, D. A., C.-Y. She, and T. Yuan (2015), Retrieving mesopause temperature and line-of-sight wind from full-diurnal-cycle Na lidar observations, *Appl. Opt.*, *54*(32), 9469–9489, doi:10.1364/AO.54.009469.
LeVeque, R. J. (2002), *Finite Volume Methods for Hyperbolic Problems*, vol. 31, Cambridge Univ. Press, Cambridge, New York.
Li, F., A. Z. Liu, G. R. Swenson, J. H. Hecht, and W. A. Robinson (2005), Observations of gravity wave breakdown into ripples associated with dynamical instabilities, *J. Geophys. Res.*, D09S11, doi:10.1029/2004JD004849.
Li, F., J. Austin, and J. Wilson (2008), The strength of the Brewer-Dobson Circulation in a changing climate: Coupled chemistry-climate model simulations, *J. Clim.*, *21*(1), 40–57.
Li, T., C.-Y. She, H.-L. Liu, T. Leblanc, and I. S. mcDermid (2007), Sodium lidar-observed strong inertia-gravity wave activities in the mesopause region over Fort Collins, Colorado (41°N, 105°W), *J. Geophys. Res.*, *112*, D22104, doi:10.1029/2007JD008681.
Li, T., A. Z. Liu, X. Lu, Z. Li, S. J. Franke, G. R. Swenson, and X. Dou (2012), Meteor-radar observed mesospheric semi-annual oscillation (SAO) and quasi-biennial oscillation (QBO) over Maui, Hawaii, *J. Geophys. Res.*, *117*, D05130, doi:10.1029/2011JD016123.
Li, Z., A. Z. Liu, X. Lu, G. R. Swenson, and S. J. Franke (2011), Gravity wave characteristics from OH airglow imager over Maui, *J. Geophys. Res.*, *116*, D22115, doi:10.1029/2011JD015870.
Lindzen, R. S. (1981), Turbulence and stress owing to gravity wave and tidal breakdown, *J. Geophys. Res.*, *86*(C10), 9707–9714, doi:10.1029/JC086iC10p09707.
Liou, K.-N. (2002), *An Introduction to Atmospheric Radiation*, 2nd ed., *Int. Geophys. Ser.*, vol. 84, Academic Press, San Diego, Calif.
Liu, A. Z., and G. R. Swenson (2003), A modeling study of O_2 and OH airglow perturbations induced by atmospheric gravity waves, *J. Geophys. Res.*, *108*(D4), 4151, doi:10.1029/2002JD002474.
Liu, H.-L., and S. L. Vadas (2013), Large-scale ionospheric disturbances due to the dissipation of convectively-generated gravity waves over Brazil, *J. Geophys. Res. Space Physics*, *118*, 2419–2427, doi:10.1002/jgra.50244.
Liu, X., J. Xu, J. Yue, and S. L. Vadas (2013), Numerical modeling study of the momentum deposition of small amplitude gravity waves in the thermosphere, *Ann. Geophys.*, *31*(1), 1–14, doi:10.5194/angeo-31-1-2013.
Lu, X., A. Z. Liu, G. R. Swenson, T. Li, T. Leblanc, and I. S. mcDermid (2009), Gravity wave propagation and dissipation from the stratosphere to the lower thermosphere, *J. Geophys. Res.*, *114*, D11101, doi:10.1029/2008JD010112.
Lu, X., X. Chu, W. Fong, C. Chen, Z. Yu, B. R. Roberts, and A. J. mcDonald (2015a), Vertical evolution of potential energy density and vertical wave number spectrum of antarctic gravity waves from 35 to 105 km at McMurdo (77.8°S, 166.7°E), *J. Geophys. Res. Atmos.*, *120*, 2719–2737, doi:10.1002/2014JD022751.
Lu, X., et al. (2015b), A coordinated study of 1 h mesoscale gravity waves propagating from Logan to Boulder with CRRL Na Doppler lidars and temperature mapper, *J. Geophys. Res. Atmos.*, *120*, 10,006–10,021, doi:10.1002/2015JD023604.
Molina, A. (1983), Sodium nightglow and gravity waves, *J. Atmos. Sci.*, *40*(10), 2444–2450, doi:10.1175/1520-0469(1983)040<2444:SNAGW>2.0.CO;2.
Nappo, C. (2012), *An Introduction to Atmospheric Gravity Waves, Int. Geophys.*, vol. 102, pp. 1–321, Academic Press, Amsterdam.
Picone, J. M., A. E. Hedin, and D. Drob (2002), NRLMSISE-00 empirical model of the atmosphere: Statistical comparisons and scientific issues, *J. Geophys. Res.*, *107*(A12), 1468, doi:10.1029/2002JA009430.
Sartelet, K. N. (2003), Wave propagation inside an inertial wave. Part I: Role of time dependence and scale separation, *J. Atmos. Sci*, *60*(12), 1433–1447.
She, C. Y., T. Li, B. P. Williams, T. Yuan, and R. H. Picard (2004), Concurrent OH imager and sodium temperature/wind lidar observation of a mesopause region undular bore event over Fort Collins/Platteville, Colorado, *J. Geophys. Res.*, *109*, D22107, doi:10.1029/2004JD004.742.
Smith, S. M., J. S. Friedman, S. Raizada, C. A. Tepley, J. Baumgardner, and m. Mendillo (2005), Evidence of mesospheric bore formation from a breaking gravity wave event: Simultaneous imaging and lidar measurements, *J. Atmos. Sol. Terr. Phys.*, *67*(4), 345–356, doi:10.1016/j.jastp.2004.11.008.
Snively, J. B., and V. P. Pasko (2008), Excitation of ducted gravity waves in the lower thermosphere by tropospheric sources, *J. Geophys. Res.*, *113*, A06303, doi:10.1029/2007JA012693.
Snively, J. B., V. P. Pasko, M. J. Taylor, and W. K. Hocking (2007), Doppler ducting of short-period gravity waves by midlatitude tidal wind structure, *J. Geophys. Res.*, *112*, A03304, doi:10.1029/2006JA011.895.
Snively, J. B., K. Nielsen, M. P. Hickey, C. J. Heale, M. J. Taylor, and T. Moffat-Griffin (2013), Numerical and statistical evidence for long-range ducted gravity wave propagation over Halley, Antarctica, *Geophys. Res. Lett.*, *40*, 4813–4817, doi:10.1002/grl.50926.
Suzuki, S., F.-J. Lübken, G. Baumgarten, N. Kaifler, R. Eixmann, B. P. Williams, and T. Nakamura (2013a), Vertical propagation of a mesoscale gravity wave from the lower to the upper atmosphere, *J. Atmos. Sol. Terr. Phys.*, *97*, 29–36, doi:10.1016/j.jastp.2013.01.012.
Suzuki, S., K. Shiokawa, Y. Otsuka, S. Kawamura, and Y. Murayama (2013b), Evidence of gravity wave ducting in the mesopause region from airglow network observations, *Geophys. Res. Lett.*, *40*, 601–605, doi:10.1029/2012GL054605.
Tang, J., A. Z. Liu, and G. R. Swenson (2002), H1 gravity waves observed in OH airglow at Starfire Optical Range, NM: Seasonal variations in momentum flux, *Geophys. Res. Lett.*, *29*(20), 1966, doi:10.1029/2002GL015794.
Tang, J., F. Kamalabadi, S. J. Franke, A. Z. Liu, and G. R. Swenson (2005a), Estimation of gravity wave momentum flux using spectroscopic imaging, *IEEE Trans. Geosci. Remote Sens.*, *43*(1), 103–109.

Tang, J., S. J. Franke, F. Kamalabadi, and G. R. Swenson (2005b), Motion extraction of atmospheric waves from spectroscopic imaging, *Geosci. Rem. Sens. Lett.*, *2*(2), 229–232.

Taylor, M. J. (1997), A review of advances in imaging techniques for measuring short period gravity waves in the mesosphere and lower thermosphere, *Adv. Space Res.*, *19*(4), 667–676.

Taylor, M. J., Y. Y. Gu, X. Tao, and C. S. Gardner (1995), An investigation of intrinsic gravity wave signatures using coordinated lidar and nightglow image measurements, *Geophys. Res. Lett.*, *22*(20), 2853–2856, doi:10.1029/95GL02949.

Vadas, S. L., D. C. Fritts, and M. J. Alexander (2003), Mechanism for the generation of secondary waves in wave breaking regions, *J. Atmos. Sci.*, *60*(1), 194–214, doi:10.1175/1520-0469(2003)060<0194:MFTGOS>2.0.CO;2.

Vanderhoff, J. C., K. K. Nomura, J. W. Rottman, and C. Macaskill (2008), Doppler spreading of internal gravity waves by an inertia-wave packet, *J. Geophys. Res.*, *113*, C05018, doi:10.1029/2007JC004,390.

Walterscheid, R. L., G. Schubert, and D. G. Brinkman (2001), Small-scale gravity waves in the upper mesosphere and lower thermosphere generated by deep tropical convection, *J. Geophys. Res.*, *106*(D23), 31,825–31,832, doi:10.1029/2000JD000131.

Yu, Y., and m. P. Hickey (2007), Numerical modeling of a gravity wave packet ducted by the thermal structure of the atmosphere, *J. Geophys. Res.*, *112*, A06308, doi:10.1029/2006JA012092.

Yuan, T., et al. (2016), Evidence of dispersion and refraction of a spectrally broad gravity wave packet in the mesopause region observed by the Na lidar and Mesospheric Temperature Mapper above Logan, Utah, *J. Geophys. Res. Atmos.*, *121*, 579–594, doi:10.1002/2015JD023685.

Zhang, S. D., and F. Yi (2002), A numerical study of propagation characteristics of gravity wave packets propagating in a dissipative atmosphere, *J. Geophys. Res.*, *107*(D14), 4222, doi:10.1029/2001JD000864.